Research
Textile Engineering—Article

Rotary Three-Dimensional Braider Design Method Based on the Average Cutting Circle Strategy

Xin Yang [a,b], Siyi Bi [a,b], Huiqi Shao [a,c], Chenglong Zhang [a,b], Jinhua Jiang [a,b,*], Frank K. Ko [d,*], Nanliang Chen [a,b,*]

[a] Engineering Research Center of Technical Textile, Ministry of Education, College of Textiles, Donghua University, Shanghai 201620, China
[b] Shanghai High Performance Fibers and Composites Center, Donghua University, Shanghai 201620, China
[c] Innovation Center for Textile Science and Technology, Donghua University, Shanghai 201620, China
[d] Department of Materials Engineering & AMPEL, University of British Columbia, Vancouver, BC V6T 1Z4, Canada

ABSTRACT

Three-dimensional (3D) braided composites have significant potential for use in engineering structural materials. However, conventional 3D braiding machines are insufficient for designing composites with complex geometries. This paper proposes a programmable design methodology for 3D rotary braiding machines using circle-cutting and combination strategies. By introducing varying numbers of incisions on the circle, a diverse range of horn gears can be designed. Different combinations of these cut-circles allow the horn gears to be assembled into various 3D rotary braiders. The parametric equation for the braider plate is derived, showing that a combination strategy involving two cut-circles is feasible for braider design, whereas integrating three cut-circles simultaneously is impossible for a single machine. The construction of an automatic 6-3 type 3D braiding machine demonstrates the effectiveness of the proposed design strategy. This flexible braider design approach provides a practical solution for producing 3D braided composites with complex geometries.

1. Introduction

Three-dimensional (3D) braided composites have garnered significant attention due to their exceptional mechanical properties, such as high delamination resistance, energy absorption, and damage tolerance [1–3]. These attributes, combined with their extensive application potential in the aerospace, automobile, and medical industries, make them highly valuable [4–6]. Moreover, the 3D braiding technique shows great promise in emerging fields, such as triboelectric nanogenerators (TENG) [7,8], sensors [9,10], and electrochemical cells [11,12]. A 3D braided composite typically comprises a resin matrix and a braided fabric preform, with the latter providing the primary mechanical performance as the intensifying phase [13–15].

As the use of 3D braided composites becomes more widespread, there is a growing demand for seamless integrated braiding technology capable of achieving arbitrary geometries without additional connection processes. Diverse applications necessitate various shapes of 3D braided composites, and the seamless formation of complex geometries can eliminate the need for connecting parts, such as riveting and welding, thus enhancing product reliability [16].

Current 3D braiders fall into two categories: track-and-column braiders and rotary braiders [17,18]. Track-and-column braiders, the most popular method, interlace yarns by simultaneously driving an entire line of carriers, but these limits control over individual carriers. This limitation makes it difficult to automatically braid complex structures with varying cross-sections without significant manual intervention. Additionally, track-and-column braiders rely on numerous cylinders to move carriers along horizontal or vertical paths, adding to the complexity of their mechanical structure. Consequently, track-and-column braiders are best suited for designing square cross-sectional braided reinforcements. In contrast, 3D rotary braiders excel in creating varying cross-sections due to their individually controllable horn gear mechanisms [19].

Despite notable advancements, existing 3D braiding techniques still struggle to achieve complex geometries [20–22]. Achieving the same level of geometric realization with 3D braiding technology as

* Corresponding authors.
E-mail addresses: jiangjinhua@dhu.edu.cn (J. Jiang), frank.ko@ubc.ca (F.K. Ko), nlch@dhu.edu.cn (N. Chen).

with 3D printing would represent a significant breakthrough for all engineering structural material industries [23].

The rotary 3D braider achieves precise control over each horn gear using an independent motor, allowing for accurate manipulation of yarn carriers between gears. This significantly enhances the braider's ability to design preforms, showing promising potential for further development. In 1930, Blaisdell [24] designed a machine with a unique dial array plate to braid an L-shaped 3D fabric. However, this dial device only provided forward motion for the yarn carrier, which had to follow a track engraved on the plate. Ma [25] proposed a 3D weaving method based on a triangular turntable using space group theory, but the fixed carrier track limited to ability to braid complex structures. The Geneva horn gear mechanism [26] was introduced to control carrier direction, leading to advancements in rotary 3D braiders. Tsuzuki er al. [20] was the first to introduce the Geneva horn gear to 3D braiding, creating the Tsuzuki braider. However, this machine could not rotate adjacent horn gears simultaneously. Laourine et al. [27] improved on Blaisdell's dial-type braider by adding a clutch device, resulting in the Herzog rotary 3D braider, which could change carrier tracks. Bogdanovich and Mungalov [28] further modified the Tsuzuki braider by adding a switch device between adjacent horn gears, allowing them to rotate simultaneously.

Traditional Geneva horn gears with four incisions could only carry four yarn carriers, so increasing the number of incisions allowed more yarns to be used in braiding. Refs. [29–34] introduced the concept of a hexagonal braider with horn gears featuring six incisions. The first-generation hexagonal braider, co-developed by Ko and Aachen University of Technology in Germany, increased the yarn-carrying capacity by 38% compared to the Tsuzuki braider [19]. However, it still faced the issue of adjacent horn gears not being able to rotate simultaneously. This was resolved in the second-generation hexagonal braider with the introduction of a switch device between adjacent horn gears. Li [19] experimented with designing new braiders by varying the number of horn gear incisions. However, this approach only utilized a single type of horn gear, resulting in a limited distribution pattern for the horn gears.

This study introduces a new design method for the horn gears of 3D rotary braiders using circle-cutting and arrangement strategies. By combining horn gears with different numbers of incisions, various types of 3D braiding machines can be created. Analyzing the geometry and positional arrangement of cut-circles, we established the parametric equation for the braider plate. A parametric equation program was then developed to calculate parameters for cut-circles with 2 to 8 incisions. Using this program, more than eight effective 3D rotary braider models were designed by arranging cut-circles from a basic class and extending this class with a general division angle.

Geometric analysis revealed that using a combination strategy involving three types of cut-circles is not feasible for braiding machine development. Furthermore, the new braiders, with the same number of horn gears as existing ones, can accommodate more carriers, enhancing their potential for designing and braiding complex patterns. To demonstrate this potential, a complex bifurcated pipe was designed using the new rotary braider. Additionally, a novel rotary braiding machine was constructed to validate the proposed approach. Braiding experiments showed that the machine enables automatic, microcomputer-controlled braiding of even preforms. The fabric was then consolidated into a hexagonal composite. Although there was a decrease in elongation modulus compared to traditional composites, the hexagonal composite exhibited superior mechanical properties.

2. Methodology

Fig. 1 illustrates the model of the 3D rotary braider. The xoy plane of the coordinate system represents the braiding plate, where the carriers, horn gears, and switches are positioned. The oz axis is oriented in the direction of braiding. For simplicity in parametric design, horn gears and switches are collectively referred to as cut-circles. Yarns travel at a speed of $v(t)$, in which t means time, along the oz axis and are interwoven by the motion of carriers in the xoy plane to create a braided preform. Designing the movement path of carriers on the xoy plane is critical to the movement mechanism of the 3D braider, as yarns can only travel in a straight line along the oz axis, and the preform structure is directly influenced by the controllable path of carriers. The design of the rotary 3D braiders hinges on the shape and spatial arrangement of the cut-circles on the plate, relative to the carrier movement path. The design process consists of the following steps:

(1) A MATLAB (MathWorks, USA) script generates the shape parameters of the horn gear automatically using a parameter equation with specified input parameters.

(2) Using these shape parameters, the basic class braider is designed according to an arrangement principle. To create additional braider configurations, the general division angle is used to expand beyond the basic class.

(3) The methodology was validated through the construction of a rotary prototype braider, which was used to braid a preform.
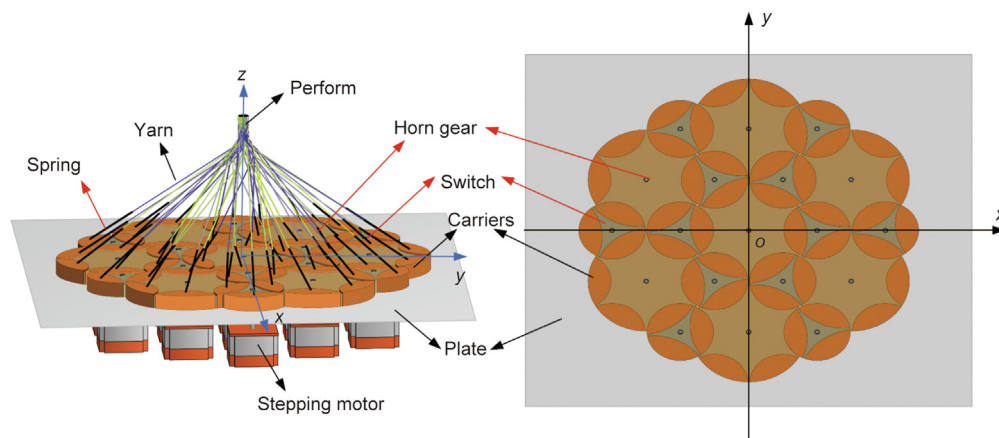

Fig. 1. Schematic diagram of the rotary 3D braider configuration.

2.1. Design method

2.1.1. Basic parameter definition

The average cutting circle method is introduced for designing the shapes of cut-circles. This method involves dividing a complete circle into n equal sectors according to the average division angle α. An incision is then made in each equal sector to create the cut-circle. The average division angle α can be calculated using Eq. (1):

$$\alpha = \frac{2\pi}{n} \tag{1}$$

where n represents the number of incisions. Fig. 2(a) demonstrates that when $n = 4$, a complete circle is divided into four equal sectors using the average cutting circle method with the average division angle $\alpha = \frac{\pi}{2}$. In this method, each equal sector is cut to create an incision, with the cutting angle β defining the size of the incision. The cutting angle is the angle between the ends of the incision curve and the center of the circle. As depicted in Fig. 2(a), $\beta = \angle eof$.

Since the size of the incision cannot exceed the area of each equal sector, the cutting angle β must satisfy $\beta \leq \alpha$. When the angle bisector of the angles α and β coincide within each equal-sector area, the circle is cut to form the incisions. Once all the equal-sector areas are cut, a "star" shape with n uniformly distributed points is produced. Fig. 2(b) illustrates a "star" with six uniformly distributed points encircled by a hexagon. This pattern, enclosed by a regular n-sided polygon, is referred to as "cut-circle with n incisions." Therefore, the shape of the cut-circle is defined as a circle with n incisions along its edges. The incision is made as a circular arc to ensure smooth rotation of the cut-circle, with the radius of the arc being equal to or greater than that of the circumcircle of adjacent cut-circles.

Each cut-circle with n incisions can accommodate up to n carriers, arranged at $\frac{2\pi}{n}$ intervals around the cut-circle, making the carrier's shape equivalent to the incision shape. The cut-circle is mounted on a fixed-area plate, with carriers positioned at the incisions. By increasing the packing density of the cut-circles, the number of carriers can be maximized, allowing for more yarns to be processed within the same space and resulting in more densely packed structures [35].

Fig. 2(b) illustrates the packing of three cut-circles. To prevent overlap between adjacent cut-circles, the sum of the internal angles $(\theta_1 + \theta_2 + \theta_3)$ of the three regular polygons must be less than or equal to 2π. For m cut-circles to be packed, their internal angles θ_i must satisfy the condition given in Eq. (2):

$$\sum_{i=1}^{m} \theta_i \leq 2\pi \tag{2}$$

where $\theta_i = \pi \times (n - 2)/n_i$ and the subscript i denotes the serial number of cut-circle. If Eq. (2) is satisfied with equality, the cut-circles can be packed without any gaps. However, if the condition is satisfied with less-than sign, a gap will exist and stationary guides must be added to the plate to direct the carrier movement through these gaps.

2.1.2. The incision design of the cut-circle

In the plate, each cut-circle must be connected to one or more adjacent cut-circles, making the incision shape of each cut-circle dependent on its neighboring cut-circles. As shown in Fig. 2(c), two adjacent cut-circles are designed as cut-circle a and cut-circle b, with their circumcircles labeled as circumcircle A and circumcircle B, respectively. The intersection of circumcircles A and B defines incision C, where the incision is made, and where a uniformly shaped yarn carrier is placed. This yarn carrier functions
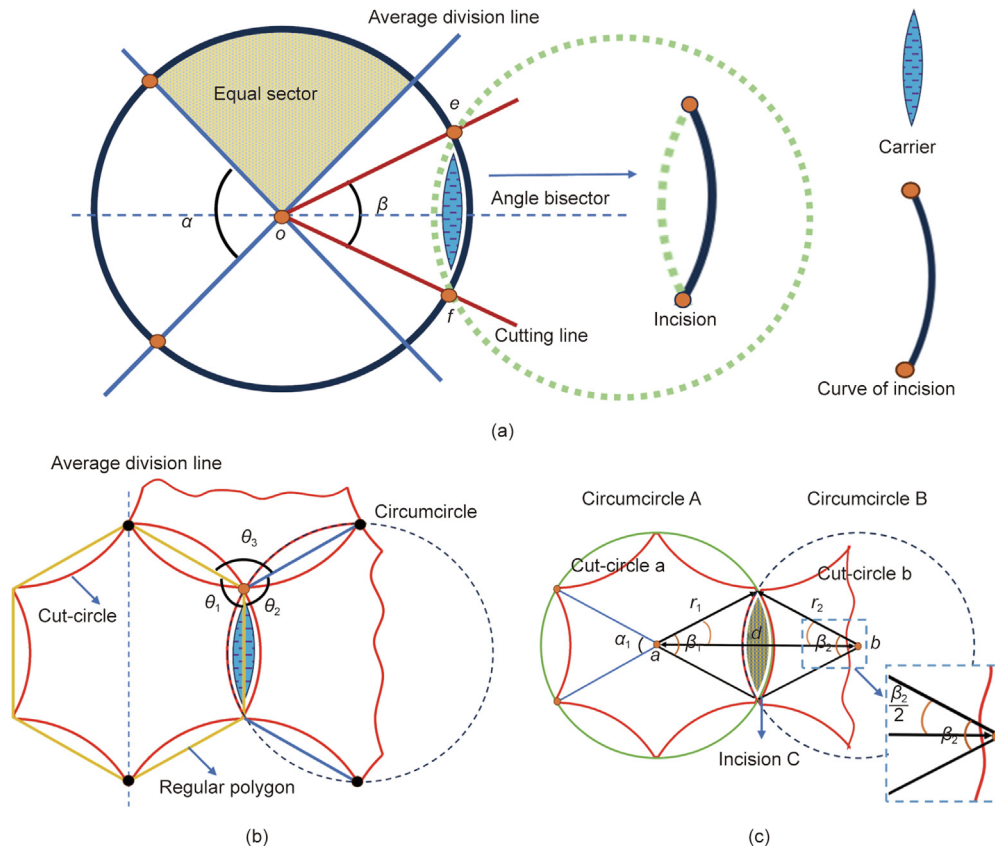

(a)

(b)

(c)

Fig. 2. Cut-circle design: (a) average circle cutting method for $n = 4$, dividing the circle into four equal sectors; (b) arrangement of cut-circles in the plate; and (c) parameters of adjacent cut-circles.

as a glider, moving according to the gripping indentation of cut-circle a (or b) as cut-circle a (or b) rotates. Because cut-circles a and b cannot rotate simultaneously to prevent collisions, a step-wise movement is required.

Since the radius of the arc on incision C is equal to that of the circumcircle of the adjacent cut-circle, the incision shape of cut-circle a at the incision C is an arc of the circumcircle B. During the braiding process, the area swept by the movement of cut-circle b corresponds to circumcircle B, and the other incisions of the cut-circle a will also rotate into the position of incision C. Therefore, to ensure the smooth rotation of cut-circle b, all the incisions on A must be identical. A circumcircle with the same radius is essential for all cut-circles in contact with circumcircle A.

The center distance d is the distance between the centers of adjacent circumcircles, adhering to the following rules:

(1) The center distance between a cut-circle and all its adjacent cut-circles is the same.

(2) The angle between two adjacent center distances corresponds to the division angle on the cut-circle.

The radius of a cut-circle is the radius of its circumcircle. For two adjacent cut-circles, the number of incisions is n_1 and n_2; the radius is r_1 and r_2; and the cutting angle is β_1 and β_2. To design an effective cut-circle, these parameters must comply with Eqs. (3)–(9) (the derivation for parameter equations in Section S1 in Appendix A).

$$\beta_1 + \beta_2 \leq \pi \tag{3}$$

$$\beta_1 \leq \frac{2\pi}{n_1} \tag{4}$$

$$\beta_2 \leq \frac{2\pi}{n_2} \tag{5}$$

$$r_2 = r_1 \cdot \sin\left(\frac{\beta_1}{2}\right) \bigg/ \sin\left(\frac{\beta_2}{2}\right) \tag{6}$$

$$d = r_1 \cdot \cos\left(\frac{\beta_1}{2}\right) + r_2 \cdot \cos\left(\frac{\beta_2}{2}\right) \tag{7}$$

$$r_1 \leq d \cdot \sin\left(\frac{\pi}{n_2}\right) \tag{8}$$

$$r_2 \leq d \cdot \sin\left(\frac{\pi}{n_1}\right) \tag{9}$$

With a fixed value of r_1, the program can be set up to calculate the range of values for the cut-circle design parameters β_1, β_2, d, and r_2. In practical applications, the cutting angle β should be as close as possible to the average division angle α to maximize cut-circle packing density. This method allows for the determination of the optimal value for d, r_2, β_1, and β_2 using MATLAB script.

2.2. Arrangement strategy

2.2.1. Arrangement hypothesis

To refine the study of arrangement, an initial hypothesis is proposed: A single cut-circle cannot be connected to two distinct types of cut-circles simultaneously (if the two types of cut-circles have the same radius, they are considered to be the same type of cut-circle). The spatial relationship among various cut-circles is examined to validate this hypothesis. The analysis is divided into two parts: the arrangement of four or more types of cut-circles and the arrangement of three types of cut-circles. These aspects are discussed in detail in the following subsections.

Arrangement of four or more kinds of cut-circles. Consider a combination of four types of cut-circles with internal angles θ_1,

θ_2, θ_3, and θ_4. For an effective and reasonable configuration, the regular polygon formed by these adjacent four cut-circles must share a common vertex. By substituting θ_1, θ_2, θ_3, and θ_4 into Eq. (2): $\theta_1 + \theta_2 + \theta_3 + \theta_4 \leq 2\pi$. Since the four internal angles are not equal, employing the four types of polygons ($n = 2, 3, 4$, and 6) with the smallest internal angles will not satisfy the equation. Consequently, an arrangement of four or more types of cut-circles does not exist.

Arrangement of three kinds of cut-circles. In the case of arranging three types of cut-circles, there must be a cut-circle X (in which "X" means that the center of the cut-circle is point X, similarly hereinafter) that is connected to two cut-circles Y and Z, with the numbers of incisions for these three cut-circles being n_1, n_2, and n_3. According to Rule (1) in Section 2.1.2, the center distances d_1 and d_2 from the center of X to the centers of the two cut-circles must be equal. Let the internal angles of the three cut-circles be θ_1, θ_2, and θ_3 and the number of the three kinds of cut-circles be m_1, m_2 and m_3, respectively. Based on Eq. (2), the internal angles must satisfy the condition $m_1 \cdot \theta_1 + m_2 \cdot \theta_2 + m_3 \cdot \theta_3 \leq 2\pi$.

When $m_1 = m_2 = m_3 = 1$, the circumcircles of the three cut-circles intersect pairwise, forming a triangle $\triangle XYZ$ by connecting the centers of the three cut-circles, as illustrated in Fig. 3(a).

Since the center distances are equal ($d_1 = d_2$), $\angle XYZ = \angle XZY$. According to Rule (2) in Section 2.1.2, the two angles ($\angle XYZ$ and $\angle XZY$) are the average division angles of cut-circles Y and Z, respectively. Based on Eq. (1), $\angle XYZ = \frac{2\pi}{n_2}$, and $\angle XZY = \frac{2\pi}{n_3}$. Solving for $n_2 = n_3$ indicates that the cut-circle Y and cut-circle Z are essentially the same type of cut-circle. This conclusion contradicts the initial assumption, thus disapproving the premise.

When $m_2 = m_3 = 1$ and $m_1 = 2$, two identical cut-circles appear in the arrangement, as illustrated in Fig. 3(b). For clarity in subsequent descriptions, they are hereafter referred to as cut-circle X and cut-circle X′. Connecting the centers of the four cut-circles (including three different types) creates four center distances: d_1, d_2, d_3, and d_4. According to Rule (1), $d_1 = d_2 = d_3 = d_4$, indicating that the configuration forms a rhombus, thus, $\angle XYX′ = \angle XZ′$. These angles formed are the average division angles of cut-circles Y and Z, as per Rule (2). Based on Eq. (1), $\angle XYX′ = \frac{2\pi}{n_2}$, $\angle XZX′\angle XZX′ = \frac{2\pi}{n_3}$. Solving for $n_2 = n_3$ reveals that cut-circles Y and Z are of the same type, which contradicts the initial premise.

Therefore, designs involving three types of cut-circles are not feasible. Eq. (2) can be expressed as follows:

$$m_1 \cdot \theta_1 + m_2 \cdot \theta_2 \leq 2\pi \tag{10}$$

In summary, a single cut-circle cannot be connected to two different types of cut-circles simultaneously.

2.2.2. Arrangement principle

In the plate, before rotation, the adjacent cut-circles must be positioned so that two incision points of the adjacent cut-circle
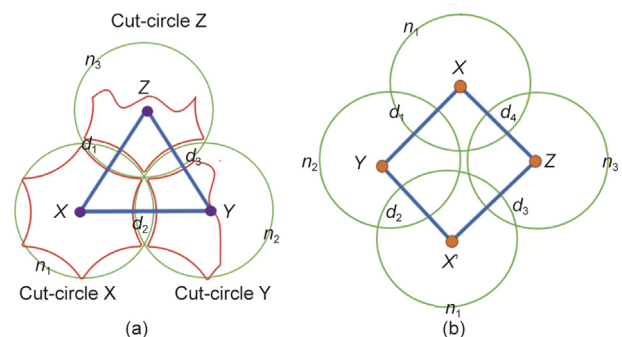

Fig. 3. Position of adjacent cut-circles. (a) Triangle of center distances; (b) rhombus of center distances.

coincide, forming a common incision point, as illustrated in Fig. 4(a). This arrangement ensures that the cut-circles rotate smoothly without collisions. Additionally, the line connecting the two common incision points must be perpendicular to the center distance, indicating that one edge of the two adjacent polygons surrounding the cut-circles must be parallel.

The arrangement principle for cut-circles dictates that any two adjacent cut-circles must be arranged as described above. As shown in Fig. 4(a), cut-circle b is connected to cut-circles a and c. These three cut-circles will create two center distances, $d_1(\overline{ab})$ and $d_2(\overline{bc})$. According to Rule (2) of the center distance in Section 2.1.2, $\angle abc$ is the division angle α. If the arrangement principle is followed, the adjacent cut-circles must be arranged as shown in Fig. 4(b), where all center distances connect to form a closed loop. This can be expressed by Eq. (11) as follows:

$$\sum_{i=1}^{m} (\pi - \alpha_i) = 2\pi \tag{11}$$

where α_i represents the average division angle and m denotes the number of cut-circle.

When $n = 2$, a special cut-circle is formed with an average division angle of π. This indicates that the cut-circle does not contribute an angle to the formation of a closed loop from the center distances. If only such cut-circles (with $n = 2$) are presented in the plate, they will be arranged along a straight line and $m \in \mathbf{N}^+$, as shown in Table 1 (Type 1).

If there is only one type of cut-circle in the plate, Eq. (11) can be expressed as follows:

$$m \cdot \left(\pi - \frac{2\pi}{n}\right) = 2\pi \tag{12}$$

Since m is a positive integer, m and n can be solved as shown in Table 1 (Type 2-4).

In Table 1, $\forall \mathbf{N}^+$ denotes any positive integer.

If there are two kinds of cut-circle in a plate, Eq. (11) can be expressed as follows:

$$m_1 \cdot \left(\pi - \frac{2\pi}{n_1}\right) + m_2 \cdot \left(\pi - \frac{2\pi}{n_2}\right) = 2\pi \tag{13}$$

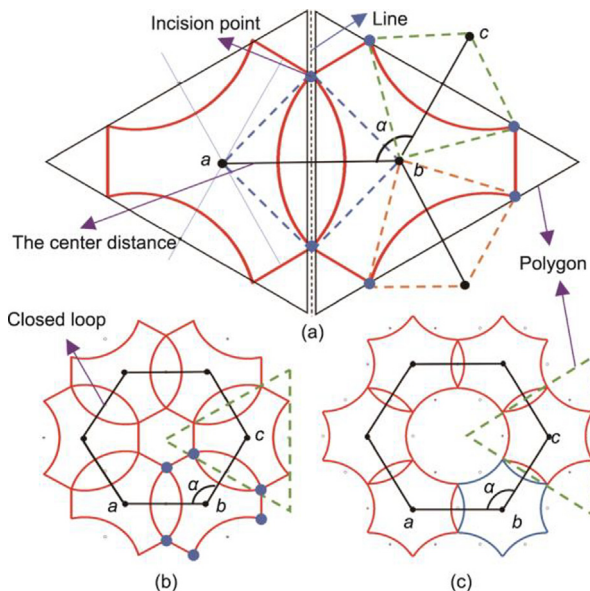Since m_1 and m_2 are positive integer, m_1, m_2, n_1, and n_2 can be solved as shown in Table 2.

Based on the proof provided earlier, a single cut-circle cannot be connected to two different types of cut-circles simultaneously, implying that m_1 and m_2 must be equal. The values of m_2 for types 6, 7, and 8 are derived from 6, 4, and 3, respectively. Therefore, only $m = 2$, 6, 7, and 8 are permissible for arranging cut-circles.

If there are three types of cut-circles in the plate, Eq. (11) can be expressed as follows:

$$m_1 \cdot \left(\pi - \frac{2\pi}{n_1}\right) + m_2 \cdot \left(\pi - \frac{2\pi}{n_2}\right) + m_3 \cdot \left(\pi - \frac{2\pi}{n_3}\right) = 2\pi \tag{14}$$

Since m_1, m_2, and m_3 are positive integers, the values for m_1, m_2, m_3, n_1, n_2, and n_3 can be determined, as detailed in Table 3.

For the arrangement of three types of cut-circles, it is inevitable that one cut-circle will be connected to two different types of cut-circles simultaneously. Therefore, arrangements involving three or more types of cut-circles are not feasible. In summary, there are only eight viable types of cut-circle arrangements. These are listed and named in Table 4.

In Table 4, the division angle γ denotes the general division angle. For any cut-circle with n incisions, provided that it meets the following criteria:

$$\frac{\gamma \cdot n}{2\pi} = k \tag{15}$$

where $k \in \mathbf{N}^+$. If two types of cut-circles have the same general division angle, one type can be substituted for the other. For example, when $n = 6$, the general division angle of a cut-circle is $\pi/3$, $2\pi/3$, or π, any class involving 2 or 3 incisions can be replaced by a cut-circle with 6 incisions. As illustrated in Fig. 4(c), a cut-circle with 6 incisions can replace a cut-circle with 3 incisions in the arrangement of the 3-class plate.

Table 1
Scheme of a single type of cut-circle.

Type	1	2	3	4
n	2	3	4	6
m	$\forall \mathbf{N}^+$	6	4	3

Table 2
Scheme of two types of cut-circles.

Type	m_1	n_1	m_2	n_2
1	3	3	2	4
2	2	3	2	6
3	4	3	1	6
4	2	4	1	8
5	1	3	2	12
6	6	3	$\forall \mathbf{N}^+$	2
7	4	4	$\forall \mathbf{N}^+$	2
8	3	6	$\forall \mathbf{N}^+$	2

Table 3
Scheme of three types of cut-circles.

Type	m_1	n_1	m_2	n_2	m_3	n_3
1	1	3	2	4	1	6
2	1	4	1	6	1	12
3	3	3	2	4	$\forall \mathbf{N}^+$	2
4	2	3	2	6	$\forall \mathbf{N}^+$	2
5	4	3	1	6	$\forall \mathbf{N}^+$	2
6	2	4	1	8	$\forall \mathbf{N}^+$	2
7	1	3	2	12	$\forall \mathbf{N}^+$	2

Fig. 4. (a) Position of two adjacent cut-circles; (b) closed loop of center distances; (c) cut-circle with 6 incisions expanding the 3-class design.

Table 4

Relationship between general division angle γ and class.

Class	2-class	3-class	4-class	6-class	6-3-class	3-2-class	4-2-class	6-2-class
n_1	2	3	4	6	3	3	4	6
n_2	–	–	–	–	6	2	2	2
γ	π	$2\pi/3$	$\pi/2$	$\pi/3$	$\pi/3, 2\pi/3$	$2\pi/3, \pi$	$\pi/2, \pi$	$\pi/3, \pi$

3. Results and discussion

3.1. Braider design

To validate the design method, this study first developed 8 basic class braiders. Subsequently, a series of braiders were created by expanding these basic class braiders using the general division angle.

3.1.1. Basic class design

As outlined in previous sections, there are only eight types of basic classes used to arrange cut-circles. For a given configuration, $r_1 = r$, where r represents the reference radius, the cutting angle β should be as close as possible to the average division angle α to achieve the optimal arrangement. Specifically, β_1, β_2, d, and r_2 can be determined using Eqs. (3)–(9) based on the optimal arrangement. These parameters are detailed in Table 5, where the first four classes represent basic class arrangements involving only one type of cut-circle, while the remaining classes involve arrangements with two types of cut-circles.

As the incisions align in adjacent cut-circles, the adjacent edges of the regular polygons formed by these cut-circles must be either parallel or coincident. When $r = 3$, the diagrams for the first four class models, illustrated in Fig. 5, can be drawn. In these diagrams, the shuttles between adjacent cut-circles represent the carriers, and the point on the shuttle denotes the positions of spindles or yarns. To prevent the jamming of adjacent cut-circles during movement, a step-wise movement approach is necessary. The basic movement mode involves the rotation of a cut-circle while keeping the surrounding cut-circles stationary. As shown in Fig. 5(a), the leftmost diagram represents the most basic unit of the plate, divided into three groups for step-wise implementation: First step, cut-circle 1 rotates 90°, while 2, 3, 4, and 5 remain stationary; second step, cut-circles 3 and 5 rotate 180°, while cut-circles 1, 2, and 4 remain stationary; third step, cut-circle 1 rotates 90°, while cut-circles 2, 3, 4, and 5 remain stationary; fourth step, cut-circles 2 and 4 rotate 180°, while cut-circles 1, 3, and 5 remain stationary. This sequence completes one rotation cycle. Fig. 5(b) illustrates the 3-class model, where one cut-circle moves while the surrounding three cut-circles remain stationary. Fig. 5(c) depicts the 4-class model, representing the Tsuzuki braider model [20], where one cut-circle rotates while the surrounding four cut-circles remain station-

ary. Fig. 5(d) shows the 6-class model, which represents the first-generation hexagonal braider model [35]. In this model, smooth rotation of one cut-circle is achieved while keeping the surrounding six cut-circles stationary.
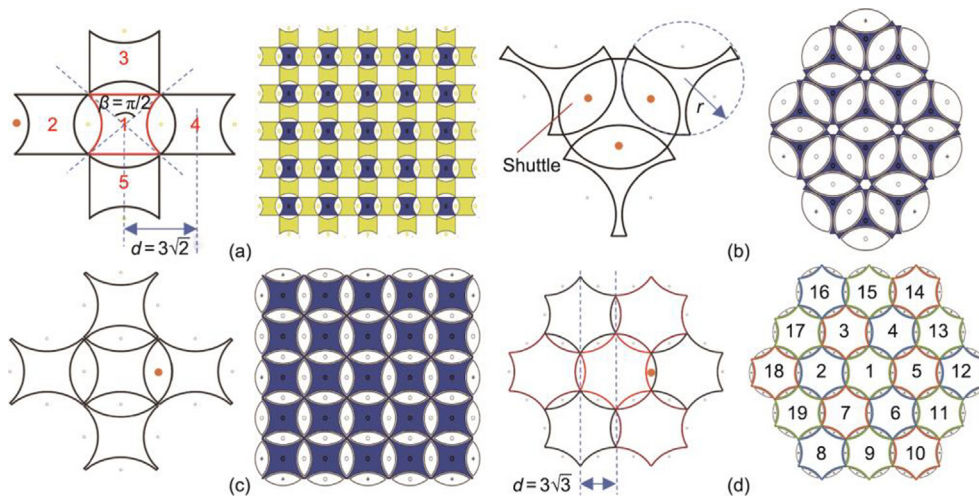
The basic class arrangements involving two types of cut-circles are illustrated in Fig. 6, with their parameters listed in the last four classes of Table 5. For these classes, cut-circles can be readily divided into two groups based on the number of incisions. The movement mode of the most basic unit of the plate involves rotating cut-circles with different numbers of incisions in an alternating fashion. For example, in Fig. 6(a), the 3-2-class features two groups of cut-circles: one with 3 incisions and the other with 2 incisions, rotating alternately. The rotation angles are integer multiples of the respective central angles of $2\pi/3$ and π. Figs. 6(b)–(d) illustrate 3-6-class, 4-2-class, and 6-2-class, respectively. Notably, the 4-2-class corresponds to the plate of the 3TEX braider [28], while the 6-2-class represents the plate model of the second-generation hexagonal braider [36].
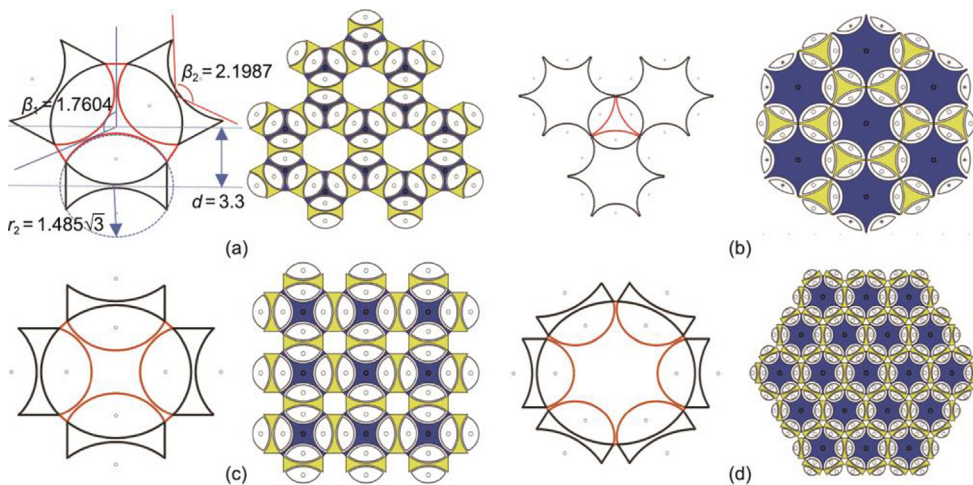
3.1.2. Expansion design

The expansion arrangement is based on the general division angles. Considering Eq. (15), the relationship between the number of incisions (n) and the general division angles (γ) is presented in Table 6.

Since $k \in \mathbf{N}^+$, countless arrangements can be designed theoretically, as shown in Table 6. However, for practical purposes, only several representative expansion arrangements are selected in this paper. The parameters of these expansion arrangements are determined using Eqs. (3)–(9) and are listed in Table 7.

When $n = 8$, the general angle $\gamma = \pi/2$ can be determined from Table 6, indicating that the cut-circle with 8 incisions belongs to the 4-class. Therefore, the cut-circle with 8 incisions can replace the cut-circle with 4 incisions to extend 4-class, forming a new plate designated as 8. The parameters for this arrangement are listed in the first row of Table 7, with Fig. 7(a) depicting the plate. The movement mode for the basic unit of the plate involves dividing the entire plate into two groups to ensure no two adjacent cut-circles rotate simultaneously. During the braiding process, the two groups of cut-circles move alternately; for example, one group rotates $2\pi/8$ counterclockwise, while the other rotates $2\pi/8$ clockwise. Similarly, the cut-circle with 4 incisions, whose general angle $\gamma = \pi/2$ can replace the cut-circle with 2 incisions, expands the 3-2-class to form the 3-4 plate. The parameters for this

Table 5

Parameters of basic arrangements.

Class	d	β_1	β_2	r_2
2	$\sqrt{2}r$	$\pi/2$	–	–
3	$\sqrt{2}r$	1.8692	–	–
4	$\sqrt{2}r$	$\pi/2$	–	–
6	$\sqrt{3}r$	$\pi/3$	–	–
3-2	$1.1r$	1.7604	2.1987	$0.495\sqrt{3}r$
3-6	$2.0r$	$2\pi/3$	$\pi/3$	$\sqrt{3}r$
4-2	$1.1r$	1.3465	2.1978	$0.495\sqrt{2}r$
4-6	$1.1r$	0.9329	2.2795	$0.495r$

Fig. 5. Basic class arrangements for single cut-circle types. (a) Plate with cut-circles having two incisions; (b) plate with cut-circles having three incisions, divided into two groups with alternating rotations; (c) Tsuzuki braider plate with cut-circles having four incisions, divided into two alternating rotation groups; (d) first-generation hexagonal braider plate with cut-circles having six incisions, divided into three alternating rotation groups for yarn interweaving.

Fig. 6. Basic class arrangement of two kinds of cut-circle. (a) Assembly of cut-circles with three incisions and two incisions; (b) assembly of cut-circles with three incisions and six incisions, with alternating rotations; (c) assembly of cut-circles with four incisions and two incisions, with each type rotating alternately, the rotation angles are integer multiples of their corresponding central angles of $\pi/2$ and π; (d) assembly of cut-circles with four incisions and cut-circles with two. Cut-circles with 6 incisions are in one group, while those with 2 incisions are in another group. The two groups of cut-circles are rotated alternately, and the rotation angles are integer multiples of their corresponding central angles of $\pi/3$ and π.

Table 6
Relation between general angle γ and the number of incision n.

γ	π	$2\pi/3$	$\pi/2$	$\pi/3$
n	$2k$	$3k$	$4k$	$6k$

configuration are listed in the second row of Table 7. Fig. 7(b) illustrates the expansion arrangement and the new plate.

The remaining expansion designs in Table 7 are depicted in Fig. 8, according to their corresponding parameters. In these designs, the cut-circles can be divided into two groups based on the number of incisions, utilizing a step-wise movement to prevent jamming of the adjacent cut-circles during motion.

3.2. Comparison of 3D rotary braiders

Different arrangements of cut-circles lead to various braiding structures, which can be systematically categorized using the n_1–n_2 type notation. Where, n_1 and n_2 represent the number of incisions on the horn gear and the switch, respectively. For example, a plate with only one type of cut-circle with 3 incisions is designated as type 3-3, while a combination of a cut-circle with 3 incisions and another with 4 incisions is referred to as type 3-4. Ten types of new braiders are summarized in Section S2 in Appendix A and four types of existing braiders in Section S3 Appendix A [20,28,36].

Sections S2 and S3 summarize the features of the 3D rotary braider, including characteristics, such as the arrangement of horn gears and switches, simulation of braider, carrier positions, and preform configuration. In contrast to the four types of existing braiders that can only move one or two carriers between two adjacent horn gears, these new braiders enable the positioning of more carriers by incorporating different switches between adjacent horn gears, thereby maximizing the potential number of carriers. For instance, the 6-4 type can move four carriers between two adjacent horn gears, which is twice as many as the 6-2 type braider of a similar type.

Table 7
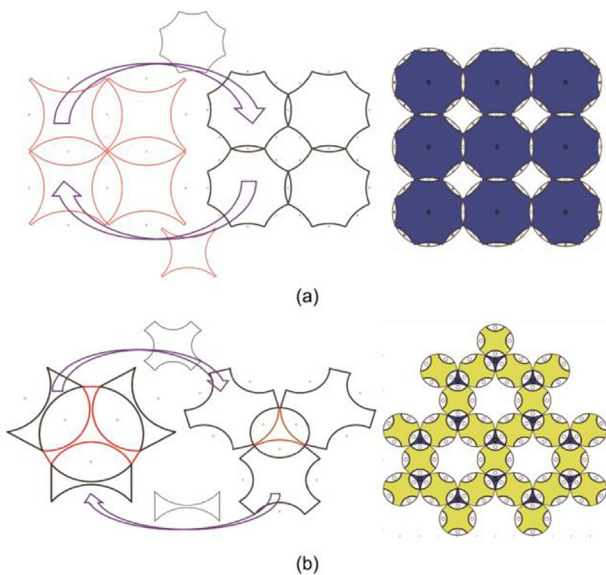Parameters of expansion arrangements.

Class	Expansion	d	β_1	β_2	r_2
4	8	$2r \cdot \cos(\pi/8)$	$\pi/4$	—	—
3-2	3-4	$2r$	$2\pi/3$	$\pi/3$	$\sqrt{3}r$
3-2	3-8	$2.5838r$	2.0561	$\pi/4$	$2.2376r$
4-2	4-6	$1.906r$	1.4789	$\pi/3$	$1.3478r$
4-2	4-8	$2.2737r$	1.3254	$\pi/4$	$1.6077r$
6-2	6-4	$1.3560r$	0.9948	1.5708	$0.6748r$

Fig. 9 illustrates the relationship between the number of carriers and the number of horn gears. Fig. 9(a) demonstrates that the carrier number for 3-class braiders with 18 horn gears increases

Fig. 7. Expansion arrangement process. (a) Expanding 4-class, (b) expanding 3-2-class; cut-circles of 3 and 4 incisions rotating alternately at integer multiples of their central angles of $2\pi/3$ and $2\pi/4$.
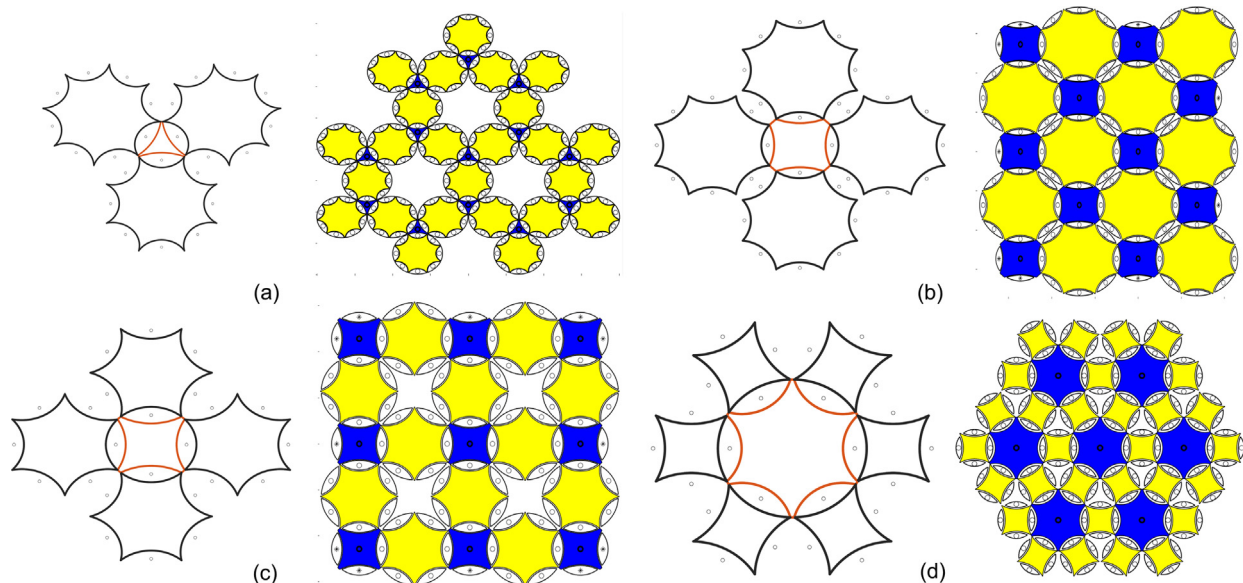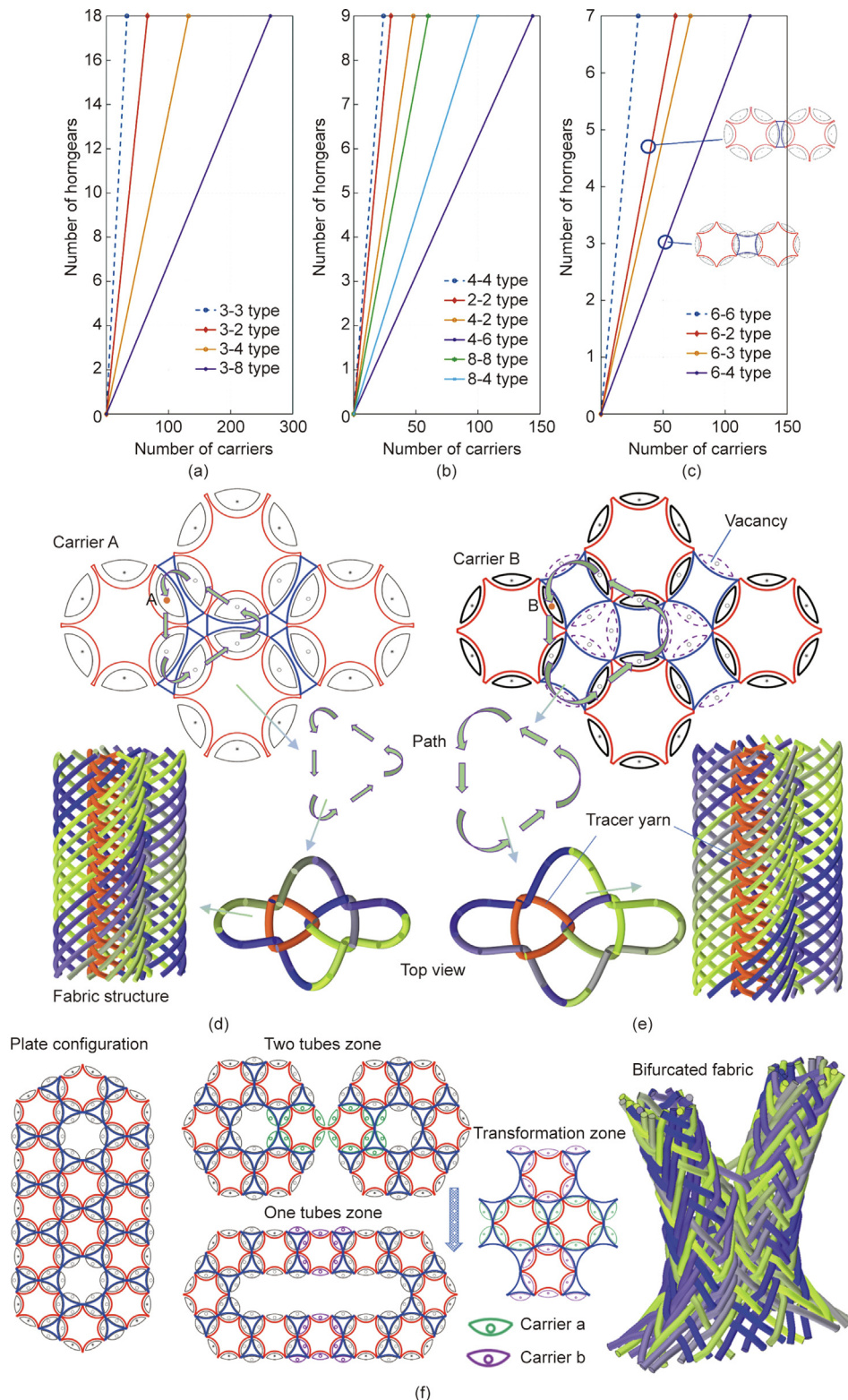
rapidly with the number of switch incisions, with the carrier number for the braider (3-3 type) without a switch being the minimum. For example, a 3-8 type braider with 18 horn gears can hold 264 carriers, which is eight times more than the 3-3 type. This trend is also evident in Figs. 9(b) and (c). Due to switch limitations, existing braiders hold fewer carriers than new braiders (except for the 2-2 type), as shown in Figs. 9(b) and (c). Therefore, new braiders capable of holding more carriers show great potential for designing and braiding complex patterns.

To confirm the effectiveness of the proposed method for enhancing the braiding function of the braider, a control experiment was conducted using the 6-2 type braider and its expanded design, the 6-4 type. As depicted in Fig. 9(d), the plate configuration of the 6-2 type includes four cut-circles with 6 incisions and five cut-circles with 2 incisions. In contrast, the 6-4 type replaces the cut-circles with 2 incisions with cut-circles with 4 incisions, as illustrated in Fig. 9(e). For the 6-4 type, some carriers—indicated by dotted lines in Fig. 9(e)—are vacant and do not place yarn to maintain the same number of carriers as the 6-2 type.

Both plates utilize the same movement pattern: The cut-circle with 6 incisions rotates $2\pi/6$ clockwise, while those with 2 and 4 incisions rotate $2\pi/2$ counterclockwise. Tracer carriers A and B follow identical movement paths, indicating a certain uniformity between the two braiders. The tracer yarn also reveals an identical topological structure in the top view. By comparing the fabric structures, it is evident that both configurations can produce the same fabrics, demonstrating that the 6-4 type can achieve all the braiding functions of the 6-2 type through reconfiguring the

Fig. 8. Expansion arrangements. (a) Three and eight incisions rotating alternately, the rotation angles are integer multiples of their respective central angles, $2\pi/3$ and $2\pi/8$; (b) four and eight incisions, the rotation angles are integer multiples of their respective central angles, $2\pi/4$ and $2\pi/6$; (c) four and six incisions, the rotation angles are integer multiples of their respective central angles, $2\pi/4$ and $2\pi/8$; (d) six and four incisions, the rotation angles are integer multiples of their respective central angles, $2\pi/6$ and $2\pi/4$.

cut-circles. Therefore, it is clear that the expansion design retains all the functions of the original class while introducing new braiding capabilities. This expansion not only increases the number of carriers but also enhances the braiding function. With further expansion, the braider can theoretically create richer and more complex patterns.

The bifurcated tube, commonly used in commercial artificial blood vessels [37–39], poses challenges for production with traditional braiders due to the complexity of manufacturing variable-section structures. However, 3D rotary braiders offer a significant advantage in this area due to their individually controllable horn gear mechanisms. This study proposes a method for designing

Fig. 9. Relationship between the number of horn gears and the number of carriers: (a) 3-class, (b) 4-class, and (c) 6-class braider. The comparison between (d) fabric braided by 6-2 type and (e) 6-4 type braider. (f) The design of bifurcated fabric is based on a 6-3 type braider.

bifurcated tubes using the 6-3 type rotary braider. The plate configuration for this design includes 14 cut-circles with six incisions, 30 cut-circles with three incisions, and 96 carriers, as illustrated in Fig. 9(f). During the braiding process, the braider alternates between three distinct zones to fabricate the bifurcated tube: the two-tube zone, the transformation zone, and the one-tube zone. In the two-tube zone, the plate configuration consists of 12 cut-circles with six incisions and 24 cut-circles with three incisions, organized into two groups to braid two separate tubes. In contrast, the one-tube zone utilizes a closed-loop arrangement with 12 cut-circles with six incisions and 24 cut-circles with three incisions to braid a single tube. The transformation zone facilitates the movement of carriers from their current positions to new positions, enabling the braider to switch configurations. Different colors are used to denote carrier positions: carrier a (green) represents the current position, while carrier b (purple) denotes the next position. The individually controllable horn gear mechanism allows for a smooth transition of carriers from position carriers a to b. Consequently, the braider can seamlessly transition between configurations, allowing for the effective braiding of bifurcated fabric.
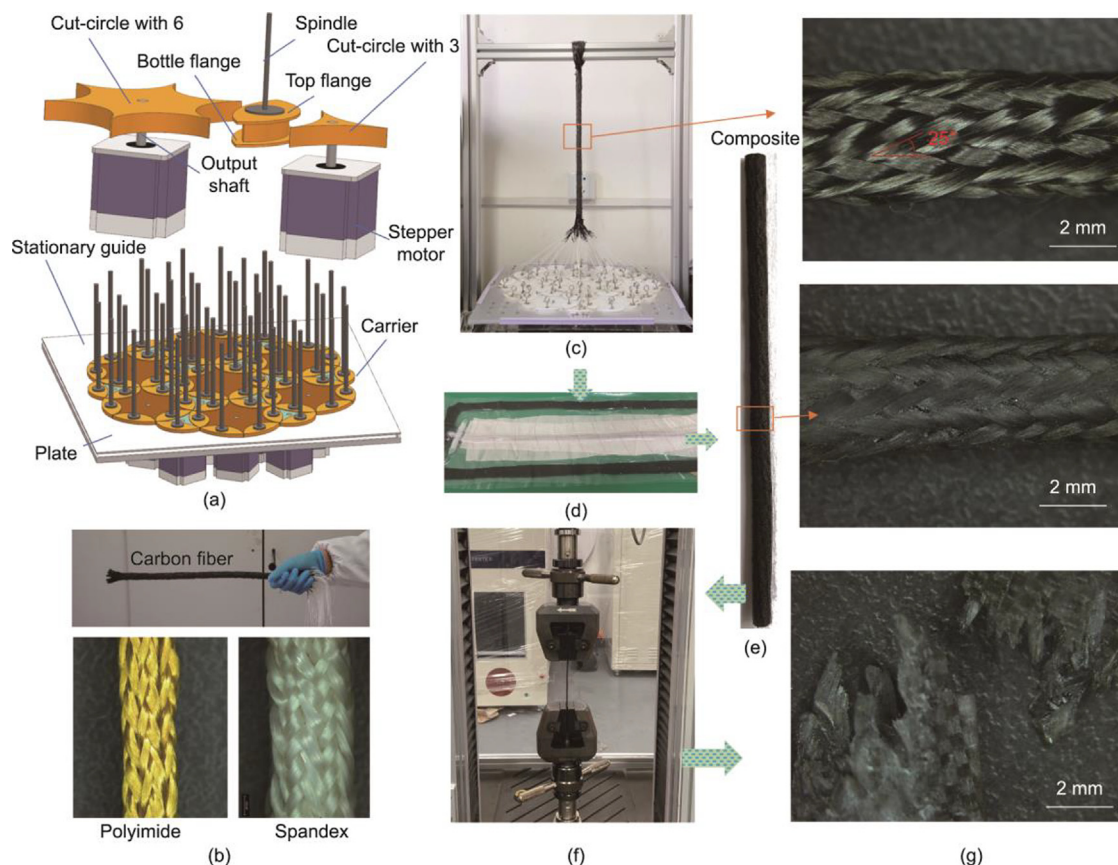
3.3. Validation

To validate the proposed methodology, a prototype 6-3 type rotary 3D braider was constructed for preform production. Fig. 10(a) illustrates the assembly drawing of the 6-3 type rotary 3D braider. This prototype includes 19 cut-circles with three and six incisions, each controlled independently by 19 stepping motors. The setup is housed in a plate or stationary guide that accommo-dates 48 carriers and 48 spindles. Additionally, each cut-circle features an axial yarn carrier fixture, allowing for the attachment of 19 axial yarn carriers, resulting in a total capacity of up to 67 carriers within a 1.6 m² area.

The design positions the cut-circles with six incisions at each cut location of the cut-circles with three incisions. Each cut-circle is connected to the output shaft of a stepping motor, which is mounted beneath the plate through multiple motor holes. The carriers, positioned at the cut locations on the cut-circles, are linked to spindles and equipped with top and bottom flanges to secure them in place between the cut-circles. The stationary guide features openings shaped to match the movement path of the outermost carrier, and its thickness corresponds to that of the cut-circles.

As detailed in Fig. 10(a), a 6-3 type 3D prototype braider was constructed. This device includes 7 cut-circles with 6 incisions and 12 cut-circles with 3 incisions. The braiding cycle was programmed such that the cut-circles with 6 incisions rotate by 60°, 0°, −60°, and 0°, while the cut-circles with 3 incisions rotate by 0°, 120°, 0°, and −120°. By repeating this cycle, the prototype braider successfully produced three different fabrics using various materials: 2200D spandex, known for its excellent rebound properties, soft 0.5K-500D polyimide fiber, and T700-12K carbon fiber filament yarn prepreg, which hardens over time. These results are shown in Fig. 10(b). Fig. 10(c) demonstrates the braiding process of the prototype and includes an optical image of the fabric braided with T300B-3000 carbon fiber filament yarns. During this process, a 2200D spandex yarn was used as a tension device. The uniformity of the fabric structure was assessed by measuring variations in surface braiding angle along the braiding axis and diameter. Table 8

Fig. 10. The validation of 6-3 type 3D rotary braider. (a) Braider assembly drawing; (b) three fabrics braided by braider using T700-12K carbon fiber filament yarns, 0.5K-500D polyimide fiber, and 2200D spandex, respectively; (c) braider and fabric structure braided by T300B-3000 carbon fiber filament yarns; (d) resin transfer molding (RTM) used to manufacture; (e) composite consisting of fabric braided by T3000B carbon fiber filament yarns and YT-CC302S epoxy resin; (f) tensile test using MTS-30KN; (g) the optical image of the fracture of composite.

lists the diameter variance ranging from 0.0612 to 0.4375 and braiding angle variations from 0.2449 to 0.5306. These results indicate that the fabrics produced exhibit consistent structure, whether using soft, hard, or high-rebound materials. Therefore, the prototype braider is capable of producing uniform structures with a diverse range of materials.

Fig. 10(d) illustrates the process of preparing T300B fabric with a surface braiding angle of 24.8°, made from 48 T300B-3000 carbon fiber filament yarns. The fabric was converted into prepreg using YT-CC302S epoxy resin (Kunshan Yituo Composite Materials Co., Ltd., China) through resin transfer molding (RTM). This method involves vacuum impregnation to remove air from the fabric's pores and then fill them with epoxy resin. The prepreg was then cured in an oven at 80 °C for 2 h, resulting in a hexagonal composite with a volume fraction of 45.13%, as shown in Fig. 10(e). A uniaxial tensile test was conducted on the hexagonal composite using an MTS-30KN machine (Mechanical Testing & Simulation, China), as depicted in Fig. 10(f), to evaluate its mechanical properties. Fig. 10(g) shows the fracture angle of the composite, indicating that the yarns did not fully align with the tensile load during the test. The stress–strain curve of the composite, presented in Fig. 11, reveals a tensile strength of 778.5298 MPa and an elongation modulus of 34.669 GPa. In comparison, T300B-3000 carbon fiber filament yarns have a tensile strength of 3530 MPa and an elongation modulus of 230 Gpa, which is provided by manufacturer. The substantial decrease in composite properties is attributed to the yarns being angled relative to the tensile axis.

The preform with a 21° braiding angle, manufactured using the 1 × 1 track and column braiding technique, was consolidated into a track-and-column composite with a volume fraction of 45% [40]. This composite exhibited a tensile strength of 665 MPa and an elongation modulus of 71.1 GPa, as shown in Fig. 11. Compared to the hexagonal composite, which demonstrates a 17.07% increase in tensile strength but a 51.24% decrease in elongation modulus,

the track-and-column composite shows superior elongation properties. The reduced elongation modulus in the hexagonal composite is mainly due to the discrepancy between surface and inner braiding angles, with the inner braiding angle being larger. Despite the lower elongation modulus, the hexagonal composite maintains favorable mechanical properties.

4. Conclusions

This study presented a novel cutting circle method for designing horn gears in 3D rotary braiding machines. It was found that by optimizing the shape and positional arrangement of the cut-circles, a diverse array of 3D braiding machines can be developed. The research involved calculating the parameters for various types of braiding machines by formulating parametric equations for the braiding machine plates. Geometric analysis showed that combining two types of horn gears leads to the creation of a wide range of new braiding machines while combining three types proved ineffective for braiding machine development. Additionally, comparing various braiders with the same type of horn gear revealed that the number of carriers increases significantly with the number of incisions in the switch. Consequently, it was found that new braiders with more incisions can accommodate more carriers than existing models, allowing for the production of more complex preforms. The 6-3 type braider was successfully used to design a complex bifurcated pipe, showcasing the rotary braider's potential for creating complex geometric textile composites. Furthermore, a new 6-3 type braiding machine was developed, capable of automatically and efficiently braiding 3D braided preforms with a uniform structure. This study offered a solution for advancing the development of complex geometric textile composites. However, as braider size increases, constructing an individually controllable motor system poses a challenge, with reducing the total power consumption of these motors being a critical issue for industrial-scale production. Future research should focus on enhancing the control scheme and software design for braiding machines.

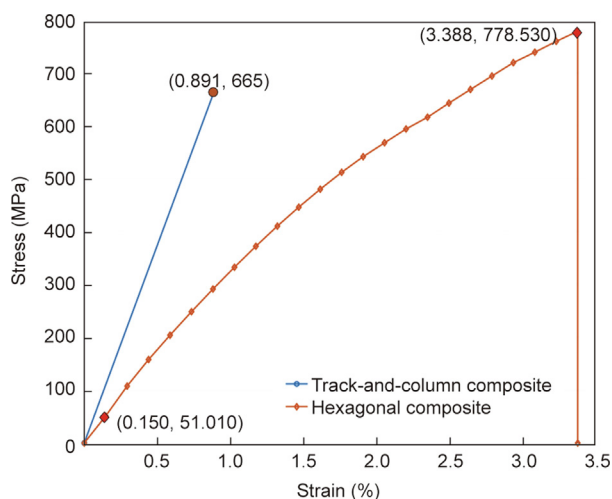## CRediT authorship contribution statement

Xin Yang: Writing – review & editing, Writing – original draft, Visualization, Software, Methodology, Investigation, Conceptualization. **Siyi Bi:** Writing – review & editing, Supervision. **Huiqi Shao:** Supervision. **Chenglong Zhang:** Writing – review & editing, Investigation. **Jinhua Jiang:** Writing – review & editing, Supervision, Funding acquisition. **Frank K. Ko:** Writing – review & editing, Supervision. **Nanliang Chen:** Supervision.

Declaration of competing interest

The authors declare that they have no known competing financial interests or personal relationships that could have appeared to influence the work reported in this paper.

Acknowledgments

Table 8
The diameter and surface braiding angle of fabrics.

Material	Diameter (mm)		Surface braiding angle (°)	
	Mean value	Variance	Mean value	Variance
T700-12K carbon	16.750	0.4375	16.8	0.4082
Polyimide	2.2857	0.0612	14.5	0.2449
Spandex	6.4286	0.2449	23.6	0.5306
T300B-3000 carbon	4.1429	0.4082	24.8	0.4722

Fig. 11. Stress–strain curve of composite.

Appendix A. Supplementary data

Supplementary data to this article can be found online at https://doi.org/10.1016/j.eng.2025.03.015.

References

[1] Ge L, Li HM, Zhong JH, Zhang C, Fang DN. Micro-CT based trans-scale damage analysis of 3D braided composites with pore defects. Compos Sci Technol 2021;211():108830.

[2] Wang RQ, Zhang L, Hu DY, Liu X, Cho CD, Li B. Progressive damage simulation in 3D four-directional braided composites considering the jamming-action-induced yarn deformation. Compos Struct 2017;178:330–40.

[3] Zhou HL, Li C, Zhang LQ, Crawford B, Milani AS, Ko FK. Micro-XCT analysis of damage mechanisms in 3D circular braided composite tubes under transverse impact. Compos Sci Technol 2018;155:91–9.

[4] Zuo HM, Li DS, Jiang L. Experimental study on compressive fatigue behavior and failure mechanism of 3D five-directional braided composites. Compo Part A 2020;139:106097.

[5] Ge JR, He CW, Liang J, Chen YF, Fang DN. A coupled elastic–plastic damage model for the mechanical behavior of three-dimensional (3D) braided composites. Compos Sci Technol 2018;157:86–98.

[6] Jiang C, Wang K, Liu Y, Zhang C, Wang B. Application of textile technology in tissue engineering: a review. Acta Biomater 2021;128:60–76.

[7] Dong K, Peng X, An J, Wang AC, Luo J, Sun B, et al. Shape adaptable and highly resilient 3D braided triboelectric nanogenerators as E-textiles for power and sensing. Nat Commun 2020;11(1):2868.

[8] Zhang C, Wu S, Narayana H, Ke Y, Shao H, Zabihi E, et al. Programmable 3D bifurcated braided structures for system-adaptable and integrated triboelectric sensing. Nano Energy 2023;118:109008.

[9] Wan ZK, Guo JM, Jia MR. Damage detection of three-dimensional braided composite materials using carbon nanotube thread. Sci Eng Compos Mater 2017;24(2):213–20.

[10] Li J, Wang L, Wang X, Yang Y, Hu Z, Liu L, et al. Highly conductive PVA/Ag coating by aqueous in situ, reduction and its stretchable structure for strain sensor. ACS Appl Mater Interfaces 2020;12(1):1427–35.

[11] Zhao C, Farajikhah S, Wang C, Foroughi J, Jia X, Wallace GG. 3D braided yarns to create electrochemical cells. Electrochem Commun 2015;61:27–31.

[12] Shi B, Li L, Chen A, Jen TC, Liu X, Shen G. Continuous fabrication of $Ti_3C_2T_x$ MXene-based braided coaxial zinc-ion hybrid supercapacitors with improved performance. Nano-Micro Lett 2022;14(1):34.

[13] Guyader G, Gabor A, Hamelin P. Analysis of 2D and 3D circular braiding processes: modeling the interaction between the process parameters and the pre-form architecture. Mechanism Mach Theory 2013;69:90–104.

[14] Gu QJ, Quan ZZ, Yu JY, Yan JH, Sun BZ, Xu GB. Structural modeling and mechanical characterizing of three-dimensional four-step braided composites: a review. Compos Struct 2019;207:119–28.

[15] Arianpour M, Johari MS, Dabiryan H. Investigation on Poisson's ratio of tubular braid's structure, considering different structural deformation regimes, part 1: experimental study. J Textil Inst 2022;113(10):2227–37.

[16] Sun J, Zhou GM, Zhou CW. Microstructure and mechanical properties of 3D surface-core 4-directional braided composites. J Mater Sci 2015;50(22):7398–412.

[17] Bogdanovich AE. An overview of three-dimensional braiding technologies. In: Kyosev Y, editor. Advances in braiding technology. Sawston: Woodhead Publishing; 2016. p. 3–78.

[18] Bilisik K, Sahbaz Karaduman N, Bilisik N. Applications of braided structures in transportation. In: Rana S, Fangueiro R, editors. Braided structures and composites. Boca Raton, FL: CRC Press; 2015. p. 255–95.

[19] Li Z. Study on the forming principles of 3D hexagonal braided fabric and its composite properties [dissertation]. Shanghai: Donghua University; 2019. Chinese.

[20] Tsuzuki M, Kimbara M, Fukuta K, inventors. Three-demensional fabric woven by interlacing threads with rotor driven carriers. United States patent US 5067525a. 1991 Nov 26.

[21] Wang Y, Liu ZG, Wei YC, Li ZJ, Yi YP, Wang YB. Novel processing technology and mesoscopic geometric modeling of a new three-dimensional (3D) braided composite and the study on its longitudinal mechanical properties. Compos Struct 2020;251:112525.

[22] Ghamkhar G, Johari MS, Hosseini TH. An experimental and theoretical investigation into the effect of braiding angle and combination on a tensile modulus of the tubular biaxial hybrid braids. J Ind Text 2022;51(1 Suppl):S822–41.

[23] Ichihara N, Ueda M. 3D-printed high-toughness composite structures by anisotropic topology optimization. Compos Part B Eng 2023;253:110572.

[24] Blaisdell SB, inventor. Braided brake lining and machine for making same. United States Patent US 1885676. 1932 Jan 11.

[25] Ma W, inventor. Space group P3 symmetry based three-dimensional braiding process and technology equipment thereof. Chinese Patent CN 102358990B. 2014 Feb 14. Chinese.

[26] Fletcher JC, inventor. Geneva mechanism. United States Patent US 3855873A. 1974 Dec 24.

[27] Laourine E, Schneider M, Wulfhorst B, Pickett AK. Computerunterstützte berechnung und herstellung von 3D-geflechten. In: Proceedings of the 5th International Conference on Textile Composites; 2000 Sep 18–20; Leuven, Belgium. Berlin: Springer; 2000. Germany.

[28] Bogdanovich A, Mungalov D. Recent advancements in manufacturing 3-D braided preforms and composites. Sampe J 2009;45(6):8–28.

[29] Schreiber F, Ko FK, Yang HJ, Amalric E, Gries T. Novel three-dimensional braiding approach and its products. In: Proceedings of the 17th International Conference on Composite Materials; 2009 Jul 27–31; Edinburgh, UK. Lausanne: EPFL; 2009. p. 27–31.

[30] Yan-Tao G, Frank KO, Hong HU. Computer simulation of 3D hexagonal braided structures. J Donghua Univ 2013;46(1):23–8. Chinese.

[31] Sontag T, Yang H, Gries T, Ko F. Recent advances in 3D braiding technology. In: Chen X, editor. Advances in 3D textiles. Cambridge: Woodhead Publishing; 2015.

[32] Li JY, Zhang YF, Zhang T, Yuan L, Wang C, Ren CW, et al. A matrix computing method for visualizing switchless controlled 3D hexagonal-annular rotary braiding process architecture. Polym Compos 2023;44(10):6616–33.

[33] Mei H, Han Z, Liang S, Ko FK. Process modelling of 3D hexagonal braids. Compos Struct 2020;252:112679.

[34] Li X, He X, Liang J, Song Y, Zhang L, Wang B, et al. Research status of 3D braiding technology. Appl Compos Mater 2022;29(1):147–57.

[35] Kathrin T. Development of 3-D hexagonal braiding machine procedures and characterization of braided structures [dissertation]. Aachen: RWTH Aachen University; 2010. Germany.

[36] Tilmann S. A comparison of the Cartesion braiding process and the hexagonal braiding process to produce tubular, bifurcated structures [dissertation]. Aachen: RWTH Aachen University; 2013. Germany.

[37] Su HX, Li QT, Li DG, Li HF, Feng Q, Cao XD, et al. A versatile strategy to construct free-standing multi-furcated vessels and a complicated vascular network in heterogeneous porous scaffolds via combination of 3D printing and stimuli-responsive hydrogels. Mater Horiz 2022;9(9):2393–407.

[38] Kolesky DB, Truby RL, Gladman AS, Busbee TA, Homan KA, Lewis JA. 3D bioprinting of vascularized, heterogeneous cell-laden tissue constructs. Adv Mater 2014;26(19):3124–30.

[39] Lee S, Sani ES, Spencer AR, Guan Y, Weiss AS, Annabi N. Human-recombinant-elastin-based bioinks for 3D bioprinting of vascularized soft tissues. Adv Mater 2020;32(45):2003915.

[40] Zixing L, Zhihai F, Changhe K, Zhenguo L. Studies on tensile properties of braided structural composite materials. Acta Mater Compos Sin 1999;16:129–34. Chinese.